

**Synthesis of reaction-adapted zeolite catalysts for MTO with mimics of reaction
intermediates as OSDAs**

Chengeng Li,[†] Cecilia Paris,[†] Joaquín Martínez-Triguero, Mercedes Boronat, Manuel
Moliner, Avelino Corma*

Instituto de Tecnología Química, Universitat Politècnica de València-Consejo Superior de
Investigaciones Científicas, Avenida de los Naranjos s/n, 46022 València, Spain

*Corresponding author: E-mail addresses: acorma@itq.upv.es

[†] These authors have contributed equally

Abstract

Catalysis with enzymes and zeolites have in common the presence of well-defined single active sites and pockets/cavities in where the reaction transition states can be stabilized by longer-range interactions. We show here that for a complex reaction, as the conversion of methanol to olefins (MTO), it is possible to synthesize reaction-adapted zeolites by using mimics of the key molecular species involved in the MTO mechanism. The effort has been concentrated on the intermediates of the paring mechanism since the paring is less favored energetically than the side-chain route. All the organic structure-directing agents (OSDAs) based on intermediate mimics crystallize cage-based small pore zeolitic materials, being all of them adequate to perform the MTO reaction. Among the zeolites obtained, RTH favors the whole reaction steps following the paring route and gives the highest propylene/ethylene ratio compared to traditional CHA-related zeolites (3.07 and 0.86, respectively).

The methanol-to-olefins (MTO) reaction is a commercial process that produces light olefins (C_2^- - C_5^-) from synthesis gas via methanol, using zeolite-based catalysts.^{1,2} While methanol is obtained today from synthesis gas derived from natural gas and coal, it is expected that in a future energy scenario, in which abundant and inexpensive H_2 will be obtained from water, methanol will be a key molecule to store H_2 , as well as to produce olefins and aromatics for chemicals. Despite the MTO technology has been successfully implemented, the mechanism of the reactions involved is not yet fully understood. This is due to the complexity of the process, and the fact that the product distribution and coke formation strongly depend on zeolite structure and reaction conditions.^{3,4} There is however a general consensus that the MTO reaction proceeds through an indirect hydrocarbon pool (HP) mechanism, according to which organic species initially formed from methanol during an induction period and confined within the zeolite channels and cavities, act as co-catalysts for the reaction. These HP species are repeatedly methylated by methanol or dimethylether and subsequently split off light alkenes.³⁻⁷ Aromatic polymethylbenzenes (PMBs) and their corresponding carbenium ions (MB^+),⁸⁻¹¹ as well as polymethylcyclopentenyl (MCP^+) cations,¹⁰⁻¹² have been detected by in situ ^{13}C MAS NMR spectroscopy using isotopically-labelled methanol in H-SAPO-34, H-SSZ-13, H-BEA, H-SAPO-18 and H-ZSM-5 catalysts, and have been proposed as the main components of the hydrocarbon pool in small pore zeolites containing large cavities within their structure. On the other hand, an alkene-based cycle involving methylation and cracking of olefins also contributes to the MTO process, especially in H-ZSM-5, and is the main route in unidirectional zeolites containing straight 10-ring channels, like H-ZSM-22, where spatial restrictions prevent the formation of aromatic species.^{4,13-15}

According to the aromatics-based HP mechanism, two competitive routes have been presented as possible pathways, i.e. the side-chain and the paring routes (see Figure 1).^{4,5,16-19} The side-chain path proceeds via the alkylation of the polymethylbenzene-related intermediates with methanol,

followed by side-chain elimination to form the light olefins, preferentially ethylene and propylene. The paring cycle comprises an initial ring contraction of the polymethylbenzenium cations (MB^+), followed by the expansion of polymethylcyclopentenyl cations (MCP^+), resulting in the preferential formation of propylene and butenes. The experimental observation of the two types of cations, MB^+ and MCP^+ , by in situ techniques^{10,11} and a number of theoretical²⁰⁻²³ and isotopic labelling studies,^{18,24,25} indicate the feasibility of both pathways during the MTO process.

It has been described in the literature that when small pore zeolites containing cavities in their structure are used in the MTO reaction, the product selectivity towards different light olefins as well as the catalyst lifetime are influenced by the framework structure.^{15,26,27} That observation could be explained by the ability of the cavities present in the zeolite to favor the formation of different polyalkylated aromatics depending on their size/shape. In general, small pore zeolites with very large cavities [i.e. zeolite AFX: 15.9x10.4 Å] would favor an excessive alkylation of the aromatic HP species resulting in a faster catalyst deactivation by coke formation, whereas very small cavities [i.e. zeolite LEV: 9.8x9.5 Å] would mostly preclude the HP reaction mechanisms, limiting their catalytic activity.²⁶ On the other hand, different small pore zeolite structures containing cavities with intermediate sizes, though prepared with similar crystal sizes and chemical compositions, present different selectivities towards ethylene and propylene.²⁸⁻³² For instance, the high-silica SSZ-39 (AEI, cage dimensions: 12.6x11.2 Å, $\text{C3}^-/\text{C2}^- \sim 2.4$) and RUB-13 (RTH, cage dimensions: 11.6x10.0 Å, $\text{C3}^-/\text{C2}^- \sim 3.4$) zeolites tend to give higher propylene/ethylene ratio compared to high-silica CHA (cage dimensions: 11.7x10.2 Å, $\text{C3}^-/\text{C2}^- \sim 1.0$) zeolite (see Supplementary Figure 1),^{27,28,30} though the size of the pores and cavities, especially in the case of RTH and CHA, are very close. According to these results, it could be envisioned that even small differences in the zeolite cages may stabilize in a different manner the formation of the HP aromatic intermediates shown in Figure 1, favoring the

side chain or the paring mechanism, and changing in that way the selectivity within the olefins obtained.

If this is so, it seems reasonable that if one was able to design the cage cavity within the small pore zeolite with the adequate size and/or shape for maximizing the stabilization of particular HP intermediates, the catalyst lifetime and/or the preferential selectivity towards specific light olefins could also be maximized. In this sense, we have very recently described a new ab-initio zeolite synthesis methodology based on the use of organic structure directing agents (OSDAs) that mimic the transition states of some preestablished chemical reactions. The objective was that these mimic OSDAs could drive the synthesis towards adequate zeolite structures to catalyze the preestablished chemical reactions.³³ Following this strategy, different zeolite structures were synthesized that improved the activity and/or the selectivity to target products for different industrially-relevant chemical reactions.³³

Herein, we show the synthesis of different zeolite-based MTO catalysts using mimics of the HP intermediates as OSDAs, favoring the crystallization of zeolites with adjusted cages that maximize the host-guest interactions between the inorganic framework and the polyalkylated aromatic MTO intermediates. We have focused on the proposed MTO intermediates for the paring cycle in order to direct the reaction towards the energetically less favorable route, allowing a fine-tune olefin selectivity control depending on the synthesized reaction-adapted zeolite.

Results

Zeolite synthesis and MTO performance

According to previous theoretical studies on the MTO process,^{5,10,20,23} and our own DFT calculations (Supplementary Figures 2-5), the paring route starts with a ring contraction of the polymethylbenzenium (MB⁺) cation to form either an isopropyl-alkylated intermediate (see INT1a

in Figure 1 and INT1 in Supplementary Figure 2) or a polyalkylated bicyclic intermediate (see INT1b in Figure 1 and INT1 in Supplementary Figure 3), that splits off propene generating a polymethylcyclopentenyl (MCP⁺) cation (INT3 in Figure 1, and Supplementary Figures 2 and 3). It has also been proposed that a second isomerization of INT1 via INT2 can produce isobutene and a less substituted MCP⁺ cation in two steps (see Supplementary Figures 2 and 3). After olefin release there is a ring expansion of the MCP⁺ intermediate INT3 that, in two steps, is converted into a low-alkylated MB⁺ cation (INT5 in Figure 1 and Supplementary Figure 5) which is further alkylated by two methanol molecules regenerating the initial HP species and the reaction cycle starts again.

Following the described ab-initio mimicking approach for the synthesis of reaction-adapted zeolites, we have first prepared a series of OSDAs (see Figure 2a) that mimic the key molecular species involved in the paring mechanism, i.e. INT1, INT3 and INT5. In principle, if the above OSDAs were able to crystallize small pore zeolites, they should maximize interactions between the organic molecules and the walls within the zeolite cavity. Then, the zeolite or zeolites synthesized should minimize the energy for the formation of the molecular species involved in the paring mechanism and, accordingly, increase the C_3^-/C_2^- ratio.

Taking the isopropyl alkylated or the polyalkylated bicyclic HP intermediates (see INT1a and INT1b, respectively, in Figure 1) as possible candidates involved in the ring contraction step of the paring cycle, we carried out the preparation of two OSDAs, i.e. OSDA1a and OSDA1b (see Figure 2a) as mimics. Thus, the directing effects of these OSDAs towards the crystallization of zeolites (silicoaluminates) or related-zeotypes (i.e. silicoaluminophosphates, SAPOs) were studied. In this way, a zeolite synthesis phase diagram was considered (see Supplementary Figures 6 and 7) with the following synthesis variables: Si/Al [6-15], OSDA/Si [0.2-0.4], NaOH/Si [0-0.2], H₂O/Si [3-20], and P/Al [0.8-0.9] ratios. The use of different sources of Si, Al, or P has been proposed, including pre-

crystallized zeolites, which can favor the rearrangement and crystallization of other structures sharing similar secondary building units (SBUs) in their structures.^{34,35}

Interestingly, the silicoaluminate form of the CHA zeolite, SSZ-13, was obtained using OSDA1a and OSDA1b (see Supplementary Figure 6 and 7). In the case of OSDA1a, the SSZ-13 material was crystallized only under very specific synthesis conditions (Si/Al=6, see SSZ-13 in Supplementary Figure 6). Furthermore, it should be noted that the CHA-related zeolite is the sole microporous material obtained within all the synthesis conditions studied. In contrast, OSDA1b allows the selective crystallization of SSZ-13 zeolite under broader synthesis conditions, revealing the excellent structure directing role of the OSDA1 towards the crystallization of CHA-related zeolites (see Supplementary Figure 7). The PXRD patterns of the as-prepared SSZ-13_OSDA1a and SSZ-13_OSDA1b materials confirm the crystallization of CHA as pure crystalline phase in both cases (see in Supplementary Figure 10). Elemental analyses and ¹³C CP MAS NMR spectroscopy reveal that the organic molecules remain intact within the crystallized products (see Supplementary Table 2 and Supplementary Figure 11). The calcined SSZ-13 materials show similar textural properties compared to other CHA-related zeolites reported previously in the literature (micropore volume ~0.22-0.25 cm³/g), and the chemical analysis indicate that the final Si/Al molar ratios are comparable to the initial Si/Al molar ratios introduced in the synthesis gels (~6 and ~15 for the SSZ-13_OSDA1a and SSZ-13_OSDA1b, respectively, see Supplementary Table 3). These two samples have also been studied by FE-SEM microscopy, observing that the SSZ-13_OSDA1a and SSZ-13_OSDA1b show average crystal sizes of ~200-400 nm and ~60-80 nm, respectively (see Supplementary Figure 12), and their acidity has been characterized by NH₃-TPD (see Supplementary Figure 13).

At this point, we decided to measure the catalytic activity and selectivity of the SSZ-13 zeolites obtained and compare them with those reported in the literature for the conversion of methanol into olefins. Thus, from the different SSZ-13 samples obtained with OSDA1b, we selected one

sample with a Si/Al ratio of 15 (see SSZ-13 in Supplementary Figure 7), since the standard SSZ-13 reported in the literature synthesized using N,N,N-trimethyladamantammonium (TMAda) as OSDA is usually prepared with that Si/Al molar ratio.^{36,37}

Owing to the high catalytic activity of these SSZ-13 zeolites the MTO reaction has been carried out at 350°C, with a WHSV of 0.8 h⁻¹. For comparison purposes, a standard SSZ-13 zeolite has been prepared (see physico-chemical properties for the SSZ-13_std in Supplementary Table 3). However, since the crystal size of our SSZ-13_OSDA1b is very small, a nanosized SSZ-13 has also been prepared for a fair comparison. The nanosized SSZ-13 was prepared by combining the use of TMAda as OSDA and a surfactant molecule (cetyltrimethylammonium, CTMA) as organic modifier (see physico-chemical properties for the SSZ-13_nano in Supplementary Table 3).^{37,38} As seen in Table 1, the catalytic lifetime of the SSZ-13_OSDA1a zeolite is remarkably lower than that observed for the SSZ-13_std, due to the lower Si/Al molar ratio of the former (Si/Al=6).³¹ However, the SSZ-13_OSDA1b zeolite presents comparable Si/Al molar ratios (Si/Al=15) to other related-CHA zeolites used previously in the literature for the MTO reaction, as it is the case of the SSZ-13_std and SSZ-13_nano,³⁷. As shown in Supplementary Figure 14, the SSZ-13_OSDA1b zeolite shows a very important increase of the catalyst lifetime compared not only to the standard SSZ-13 catalyst, which presents larger crystal size, but also compared to the SSZ-13 with nanosized crystallites (see Supplementary Figure 14). In fact, the dropping of methanol conversion below 95% is obtained at ~1000 min time on stream for the SSZ-13 catalyst synthesized using the mimic OSDA1b, whereas for the standard SSZ-13 and the surfactant-based nanosized SSZ-13 materials are 212 and 472 min, respectively (see Table 1). The large difference in catalyst lifetime between the two nanosized SSZ-13 materials, SSZ-13_nano and SSZ-13_OSDA1b, cannot be attributed to differences in acidity, since the NH₃ TPD desorption profiles for these two samples are equivalent, with the typical desorption peak at 400-425°C (see Supplementary Figure 13). Therefore, these results highlight the importance

of using a mimic OSDA of the HP intermediates for synthesizing a very active and stable CHA-related MTO catalyst compared to other similar SSZ-13 catalysts synthesized with the TMAda catalyst.

The second step of the pairing mechanism is the formation of the pentaMCP⁺ intermediate cation (see INT3 in Figure 1), accompanied by the formation of a molecule of propylene. According to this, we propose a pentamethylimidazolium cation as potential mimic of the pentaMCP⁺ intermediate (see OSDA3 in Figure 2a). Most interestingly, the use of OSDA3 resulted in the preferential crystallization of the RUB-13 (RTH structure, 8x8-rings) and STA-6 (SAS structure, 8-rings) when the syntheses of silicoaluminates or silicoaluminophosphates were respectively attempted (see Supplementary Figure 8). These results show the high specificity of this organic molecule towards these small-pore crystalline frameworks, both containing the presence of large cavities within their structures.

In the case of the RUB-13, we have selected a sample synthesized with a Si/Al molar ratio of ~16 (see RUB-13 in Supplementary Figure 8) for further comparisons with the above described SSZ-13 materials, whereas in the case of the silicoaluminophosphate STA-6, a preliminary screening of some of the achieved SAS-related crystalline samples within the microscope reveals a better crystal homogenization for the selected STA-6 sample (see Supplementary Figure 8).

The RUB-13_OSDA3 sample crystallizes with an average crystal size of 60-90 nm, and the STA-6_OSDA3 sample shows orthorhombic crystals with average size of 1x4 μm (see FE-SEM images in Supplementary Figure 12). Elemental analyses of the as-prepared RUB-13_OSDA3 and STA-6_OSDA3 materials indicate that, in both cases, the OSDA3 molecules remain intact within the crystals (see Supplementary Table 2). Moreover, the calcined RUB-13_OSDA3 and STA-6_OSDA3 samples show micropore volumes of 0.25 and 0.16 cm³/g, respectively, which are comparable to those reported previously in the literature for related materials.^{30,39} Chemical analyses indicate that their chemical compositions are almost identical to the initial chemical composition introduced in

their corresponding synthesis gels, resulting in a Si/Al ratio of ~16 and a Si/(Al+P) ratio of ~0.13 for the RUB-13_OSDA3 and STA-6_OSDA3, respectively.

The catalytic activity of the RUB-13_OSDA3 and STA-6_OSDA3 materials has been evaluated for the MTO reaction, as before, at 350°C with a WSHV of 0.8 h⁻¹. The lower initial methanol conversion values and much higher catalyst deactivation observed with STA-6_OSDA3 (see Supplementary Figure 18a), is a consequence of the combination of the one-dimensional pore system present within the SAS structure together with the relative large crystal sizes of the STA-6_OSDA3 (1x4µm), which increase the diffusional problems of reactants and products. Nevertheless, it is important to remark that despite the lower initial methanol conversion, the selectivity towards the desired propylene product is very high (~45%, see Supplementary Figure 18b), suggesting that the SAS-cage would be adequate to undergo the MTO reaction. The improvement of the diffusion path length by reducing the crystal size or by creating intra-crystalline mesoporosity, should increase the catalyst life.

In the case of the RUB-13_OSDA3 catalyst, it shows an improved catalyst lifetime compared to the standard SSZ-13 zeolite, and a substantially higher propylene selectivity, being the propylene/ethylene ratio (~3.1, see Table 1) much higher than for the CHA-related silicoaluminates (~0.76-0.96, see Table 1). The high selectivity when using the RUB-13_OSDA3 catalyst,^{30,40} together with the high specificity of the mimic OSDA3 towards the crystallization of the RTH zeolite, made us to propose that the RTH cavity should better stabilize the pentaMCP⁺ intermediate than other cage-based small pore zeolites, and then maximize the propylene formation through the paring route compared to other cage-based small pore zeolites. Interestingly, the presence of pentaMCP⁺ species within the RUB-13_OSDA3 catalyst was undoubtedly observed by ¹³C CP-MAS NMR spectroscopy when the MTO reaction was performed using ¹³C labelled methanol as substrate (see signals centered at 243 and 153 ppm for the RUB-13_OSDA3 material in Figure 3). Nevertheless, the

presence of a non-negligible amount of pentene and larger olefins in the products (Supplementary Figure 17) might also indicate some small contribution of the alkene-based cycle.

In the third step of the paring mechanism, there is a ring expansion of the polymethylcyclopentenyl intermediates into a low-alkylated benzene derivative followed by a further alkylation by two methanol molecules resulting in a high-alkylated benzene intermediate (see INT6 in Figure 1). Thus, we have synthesized an alkylated pyridinium cation as potential mimic of this polyalkylated benzene HP intermediate. As seen in Supplementary Figure 9, SAPO-18 (AEI structure, 8x8x8-rings) is the preferred crystalline material when OSDA6 is used as organic template. The AEI structure is highly related to CHA, since both present tri-dimensional 8-ring pores with the same framework density (15.1 T atoms per 1000 Å³) and large cavities within their structures. Nevertheless, their cages are different, being the AEI cage basket-shaped and wider at the bottom than the CHA cage, which is more symmetric (see Supplementary Figure 1).⁴¹

The selected SAPO-18 material (see SAPO-18_OSDA6 in Supplementary Figure 9) has been characterized by different techniques to unravel its physico-chemical properties. It shows an average crystal size of ~7-10 μm (see SAPO-18_OSDA6 in Supplementary Figure 12). ICP analysis reveals analogous chemical compositions to those introduced initially in the synthesis gel (see Supplementary Table 3).

The catalytic activity of the SAPO-18 material synthesized using OSDA6 has been tested for the MTO reaction at 350°C with a WSHV of 0.8 h⁻¹. For comparison purposes, a typical SAPO-34 (CHA structure), synthesized using tetraethylammonium (TEA) as OSDA (see Methods) has also been tested. The SAPO-34 material shows longer catalyst lifetimes than the SAPO-18_OSDA6 material (~440 versus ~25 min for SAPO-34_std and SAPO-18_OSDA6, respectively, see X95 in Table 1), as could be expected just by taking into account their crystal sizes (~0.5 versus ~7-10 μm for SAPO-34_std and SAPO-18_OSDA6, respectively, see Supplementary Figure 12). However, when the

product selectivities are analyzed, it can be seen that the SAPO-18_OSDA6 sample not only gives a larger C_3^-/C_2^- compared to the SAPO-34_std (~ 2.0 and ~ 1.3 for the SAPO-18_OSDA6 and SAPO-34_std, respectively, see Table 1), but also gives a much higher selectivity to C_4^- (~ 20.0 and ~ 15.0 for the SAPO-18_OSDA6 and SAPO-34_std, respectively, see Table 1).

It should be taken into account that the paring hydrocarbon pool mechanism can also favor the formation of C_4^- light olefins.²³ Therefore, it could be then expected that those zeolite structures that favor the paring route will result in higher C_3^-/C_2^- and C_4^-/C_2^- ratios. Indeed, the two materials giving a higher C_3^-/C_2^- , which are RUB-13_OSDA3 and SAPO-18_OSDA6, they also give higher C_4^-/C_2^- compared to typical SSZ-13 or SAPO-34 materials (see Table 1). It should be noted at this point that the paring route yields initially the branched C_4^- isomer, isobutene (see Supplementary Figures 2 and 3). However, due to its hindered diffusion through the small 8R windows present in the four zeotype structures obtained in this work, isobutene cannot diffuse out from the cavities. Nevertheless, it can isomerize to linear C_4^- which are able to diffuse out. Indeed, the iso- $C_4^-/n-C_4^-$ ratio in the observed products is close to zero in all catalysts studied (see Supplementary Figure 23). The fact that the only exception is the nano-sized SSZ-13 sample exhibiting the highest external surface area (see Supplementary Table 3) indicates that the iso- C_4^- products observed in the nanosized sample have been probably formed on the outer surface of the crystallites.

The results obtained up to now clearly suggest that the particular shape of the RTH and AEI cages should favor the paring hydrocarbon pool compared to another cage-based small-pore zeolite, such as CHA, that presents more symmetrical cages, where the side-chain alkylation would more easily occur. In fact, the outstanding improvement of the catalytic activity observed for SSZ-13_OSDA1b compared to other CHA-related zeolites cannot be attributed to a better stabilization of some of the hydrocarbon pool intermediates within the paring route, since the C_3^-/C_2^- and C_4^-/C_2^- ratios are comparable to those observed for standard SSZ-13 zeolites. Although we do not have a definitive

explanation for this catalytic activity improvement at present, a different spatial distribution of the acid sites within the cavities of the nanosized CHA materials related to the OSDA1b cation during the synthesis could explain the remarkable catalytic differences observed. However, further work is required to confirm or reject the hypothesis for the preferential Al siting.

DFT calculations and MTO reaction mechanisms

To get a deeper insight into the preferential stabilization within the zeolites of the different species involved in the paring and side-chain routes, DFT calculations including dispersion interactions were performed on pure silica models of the RTH and CHA cavities (see Figure 4), considering both heptaMB⁺ and 1,2,2,3,5-pentaMB⁺ cations as initial hydrocarbon pool species. The calculated interaction energies show a stronger stabilization of all intermediates and transition states involved in the paring route (structures INT0 to INT5 in Supplementary Figures 2, 3 and 5) in the RTH cavity, with calculated values between -50 and -60 kcal/mol for the first part of the mechanism (Table 2) and slightly lower, from -45 to -55 kcal/mol after split off of the olefin (Supplementary Table 4), both for heptaMB⁺ and pentaMB⁺ HP species. As regards the intermediates involved in the side-chain route, notice that while INT7 participating in the formation of ethylene is also highly stabilized by the RTH cavity, the interaction energy obtained for INT8 is more than 20 kcal/mol lower, reflecting a worse fitting of this bulkier intermediate within the RTH framework, and discarding the formation of propylene via the side-chain pathway in RTH.

The stabilization of cationic species in CHA is weaker than in RTH and depends on the degree of methylation of the HP species. Thus, the structures formed from pentaMB⁺ cation are stabilized by 40-55 kcal/mol, while the values obtained starting from heptaMB⁺ are always lower than -50 kcal/mol. It is of particular relevance the low interaction energy values obtained for the heptaMB⁺ INT0 intermediate and for the two intermediates from the side-chain route, INT7 and INT8, in CHA, all of them around 20 kcal/mol less stable than their corresponding counterparts with pentaMB⁺

cation as HP. This might be related to the 3-fold symmetry of the CHA cavity, which does not allow the planar and fully methylated heptaMB⁺ ring to have all the methyl groups pointing to 8MR windows to avoid steric repulsion. Meanwhile, in the case of the less substituted pentaMB⁺ its smaller size allows this cation to move slightly towards the bottom of the cavity thus maximizing the stabilizing dispersion interactions (see Figure 4). On the other hand, the shape of the RTH cage provides a perfect fit with all structures involved in the paring route, and only the highly substituted INT8 intermediate, generating propylene via the side-chain route, is less stabilized due to steric repulsions.

The differences between RTH and CHA are clearly evidenced in the energy profiles shown in Figure 5, which, representing a cracking process driven by entropy at high temperature, are endothermic in both catalysts. According to the DFT calculations, pentaMB⁺ cation is similarly stabilized in both zeolites, but its reactivity towards the paring route is low due to the endothermicity of the first step of this pathway producing the bi-cyclic intermediate INT1. Therefore, preferential stabilization of pentaMB⁺ should direct the reaction towards the side-chain route, generating more ethene. Further methylation of pentaMB⁺ to heptaMB⁺ cation is difficult in CHA but energetically favored in RTH, so that the whole process following the paring route is favored within RTH framework.

These data would imply that the main species composing the HP in CHA and RTH might be different: pentaMB⁺ cations and/or their partially-alkylated derivatives in the former and heptaMB⁺ cations and/or their fully-alkylated derivatives in the latter. To evaluate this point, the organic species retained within the SSZ-13_std (CHA) and RUB-13_OSDA3 (RTH) catalysts when the MTO reaction was performed using ¹³C labelled methanol as substrate, were identified using ¹³C CP-MAS NMR spectroscopy (see Figure 3). As can be observed from the NMR spectra, both structures allow the stabilization of methyl-substituted cyclopentenyl cations (see signals between 240-250 ppm and the peak at 153 ppm in Figure 3), indicating the feasibility of the paring route in the two catalysts.

However, RTH seems more selective towards the fully methylated cyclopentenyl cation (see chemical shifts of CP-1 in Supplementary Table 4), one of the key intermediates present in the paring route and which is analogous to the mimic OSDA used for its synthesis. In addition, a peak at 132 ppm due to the ring -C- of the neutral hexamethylbenzene compound (see MB-4 in Supplementary Table 4 and Supplementary Figure 24), and at 126-128 ppm associated to -CH- groups in partially alkylated methylbenzene molecules (see MB-3 in Supplementary Table 4) are observed in the spectra of RUB-13_OSDA3 (see Figure 3), which would also indicate the presence of neutral fully and partially alkylated polymethylbenzene intermediates. On the other hand, the spectrum obtained with CHA shows an important increase of the peak centered at 128 ppm compared to RTH, which could indicate a higher relative concentration of the partially alkylated methylbenzene molecules. These data would suggest the preferential stabilization of heptaMB⁺ and fully-alkylated MCP⁺ species in the RTH cavities, thus favoring the paring route and increasing the selectivity to propylene and butenes.

Conclusions

The results presented here show that the ab-initio design of zeolites for the particular industrially-relevant MTO reaction by properly selecting the OSDA molecules based on the HP intermediates proposed in the literature, is a very attractive methodology not only to design very active and selective MTO catalysts, but also to extract more fundamental knowledge about the very complex reaction mechanism.

This rationalized synthesis approach has been useful for synthesizing zeolites well-adapted for the MTO reaction and could be extended to other chemical processes presenting complex reaction mechanisms, where the ability to design very specific structured catalysts could favor the

stabilization of particular intermediates and, consequently, maximize the yield towards the desired products.

Methods

Synthesis of the OSDAs

3-hydroxy-1-isopropyl-1-methylpyrrolidin-1-ium (OSDA1a): The reaction was performed in argon atmosphere. 1-methyl-3-pyrrolidinol (13.82 g, 0.137 moles) was poured into a two-neck round flask (previously dried at 110°C) equipped with a glass condenser and stirring; and dissolved with 200 ml of anhydrous methanol. Then, 4 equivalents of 2-bromopropane (67.40 g, 0.548 moles) was added and the solution was heated over 72 hours at methanol reflux temperature. Once the reaction was finished, the solvent was removed under reduced pressure and the product was crystallized by the addition of acetone. The product was highly hygroscopic so immediately after precipitation, was filter-off under reduced pressure and dried under vacuum and heating. The resultant bromide salt was exchanged to the hydroxide form using a commercially available hydroxide ion exchange resin (Dowex SBR).

3,3,6,6-tetramethyl-3-azabicyclo[3.1.0]hexan-3-ium (OSDA1b): The synthesis of the OSDA1b was performed in nitrogen atmosphere. 6.30 g (0.057 moles) of 6,6-dimethyl-3-azabicyclo-[3.1.0]hexane was dissolved in 60 ml of cooled anhydrous methanol and poured into a two-neck round flask equipped with a glass condenser. Then, 3.95 g of K₂CO₃ (0.029 moles) was added and the solution was stirred over one hour at 0°C. The addition of iodomethane (48.67 g, 0.343 moles) was performed dropwise, maintaining the solution at low temperature. Once the crude was stabilized, the solution was left to react for 72 h at room temperature. Then, the solvent was completely removed under reduced pressure and the residue obtained was dissolved with chloroform. The inorganic salts were separated by filtration, and the organic phase was reserved. Finally, the solution was concentrated and the product was precipitated by addition of diethyl ether. The OSDA1b was filtered and dried under reduced pressure and heating. The resultant iodide salt was exchanged to the hydroxide form using a commercially available hydroxide ion exchange resin (Dowex SBR).

1,2,3,4,5-pentamethyl-1H-imidazol-3-ium (OSDA3): The OSDA3 was synthesized in atmosphere of nitrogen. 1,2,4,5-tetramethylimidazole (10.99g, 0.089 moles) was dissolved in 120 ml of anhydrous 2-propanol and then the solution was cooled in a dry ice bath. An excess of iodomethane (37.7 g, 0.266 moles) was added dropwise and the mixture was then slowly warmed to room temperature and stirred for 48 h. The solvent was then removed under reduced pressure and the product was recrystallized from an acetone-diethyl ether solution. Finally, the product was separated by filtration and dried by vacuum. The resultant iodide salt was exchanged to the hydroxide form using a commercially available hydroxide ion exchange resin (Dowex SBR).

1,2,4,6-tetramethylpyridin-1-ium (OSDA6): In a two-neck round flask previously equipped with a glass condenser, 2,4,6-trimethylpyridine (19.80 g, 0.163 moles) was dissolved with 300 ml of ethanol. The solution was cooled in an ice-bath and then, iodomethane (69.6 g, 0.490 moles) was gradually added under vigorous stirring. The crude was stabilized at room-temperature and then mixture was allowed to react 48 h at 40°C. Fine crystals were formed at the bottom of the flask. The solution was concentrated and left at 4°C for product crystallization. Finally, the OSDA6 was separated by filtration and dried under reduced pressure. The resultant iodide salt was exchanged to the hydroxide form using a commercially available hydroxide ion exchange resin (Dowex SBR).

Synthesis of zeolites

Standard SSZ-13 (SSZ-13_std) and nanosized SSZ-13 (SSZ-13_nano): These two materials have been synthesized according to the synthesis procedures described in the ref. ³⁷.

Standard SAPO-34 (SAPO-34_std): In a typical synthesis of SAPO-34, 16.4 g of an aqueous solution of tetraethylammonium (TEAOH, 35 %wt Sigma-Aldrich) hydroxide was mixed with 1.5 g of distilled water and 4.0 g of phosphoric acid (85 %wt, Aldrich). This mixture was stirred for 30 min. Secondly, 2.94 g of alumina (75 %wt, Condea) and 0.88 g of a colloidal suspension of silica (Ludox AS40 40%wt, Aldrich) were introduced in the above mixture, and the resultant gel was stirred until complete homogenization. The chemical composition of the synthesis gel was 0.09 SiO₂ : 0.25 Al₂O₃ : 0.2 P₂O₅ : 0.5 TEAOH : 10 H₂O. The crystallization was conducted at 200°C for 1 day under dynamic conditions. The solid product was filtered and washed with abundant water and dried at 100°C. The crystalline sample was calcined at 550°C in air to remove the occluded organic species.

General synthesis procedure for silicoluminate materials using the above OSDA molecules: In a typical synthesis procedure for the silicoaluminates, an aqueous solution of the organic template (OSDA) in hydroxide was firstly mixed with the proper amount of water and 20 % sodium hydroxide solution (if required). Secondly, the required amount of aluminum hydroxide (Sigma-Aldrich) and the required amount of Ludox HS-40 were added to the above mixture. The gel was kept stirring to reach a homogeneity and then the water was evaporated by heating to reach the required concentration. The final gel composition would be SiO₂ / 0.016-0.066 Al₂O₃ / 0.2-0.4 OSDA / 0-0.1 Na₂O / 3-15 H₂O. The gel was then introduced into a Teflon-lined stainless autoclave and heated to 175°C in static condition for 14 days. The synthesis conditions of different aluminosilicate zeolites are summarized in Figures S6-S9. After the crystallization procedure, the crystalline products were

filtered and washed with abundant distilled water and dried at 100°C overnight. The samples were calcined at 550 °C in air for 6 hours to properly remove the occluded organic templates.

General synthesis procedure for silicoaluminophosphate (SAPO) materials using the above OSDA molecules: In a typical synthesis procedure for the silicoaluminophosphate (SAPO) materials, an aqueous solution of the organic template (OSDA) in hydroxide was firstly mixed with the required amount of alumina (Condea Pural SB), and the mixture was kept under stirring until homogeneity was reached. Secondly, orthophosphoric acid (85%, Sigma-Aldrich) and fumed silica (Cab-O-Sil) were added to the gel. The gel was kept under stirring to reach a homogeneity and then the water was evaporated by heating to reach the required concentration. The final gel composition would be 0.1-0.2 SiO₂ / 0.25 Al₂O₃ / 0.2-0.225 P₂O₅ / 0.2-0.4 OSDA / 3-40 H₂O. The gel was then put into a Teflon-lined autoclave and heated to 175°C in static condition for 7 days. The synthesis condition of the different SAPO materials are summarized in Figures S6-S9. After the crystallization procedure, the crystalline products were filtered and washed with abundant distilled water and dried at 100°C overnight. The samples were calcined at 550 °C in air for 6 hours to properly remove the occluded organic templates.

Characterization

Powder X-ray diffraction (PXRD) measurements were performed with a multisample Philips X'Pert diffractometer equipped with a graphite monochromator, operating at 40 kV and 35 mA, and using Cu K α radiation ($\lambda = 0,1542$ nm). The chemical analyses were carried out in a Varian 715-ES ICP-Optical Emission spectrometer, after solid dissolution in HNO₃/HCl/HF aqueous solution.

The morphology of the samples was studied by field emission scanning electron microscopy (FESEM) using a ZEISS Ultra-55 microscope and by field emission transmission electron microscopy (TEM) using a JEM 2100F microscope.

Textural properties were obtained from the N₂ adsorption-desorption isotherms measured at 77 K with a Micromeritics ASAP 2020 apparatus.

The CP/MAS NMR spectrum was recorded at room temperature with a Bruker AV 400 III HD spectrometer. ¹³C CP/MAS NMR spectrum was recorded using high-power proton decoupling (tppm) with a spinning rate of 10 kHz using 3 s recycle delay. The chemical shifts were referenced to adamantane with the upfield methine peak at 38.3 ppm.

Catalytic test

MTO reaction: The catalyst was pelletized, crushed and sieved into 0.2-0.4 mm particle size. 50 mg of sample was mixed with 2 g quartz (Fluka) before being introduced into the fixed-bed reactor (7mm diameter). N₂ (30 ml/min) was bubbled in methanol hold at -17°C, giving a WHSV=0.8 h⁻¹. The catalyst was first activated with a nitrogen flow of 80 ml/min for 1 h at 540°C, and then the temperature was decreased to reaction conditions (350°C). Each experiment was analyzed every 5 minutes with an online gas chromatograph (Bruker 450GC, with PONA and Al₂O₃-Plot capillary columns, and two FID detectors). Conversion and selectivities were considered in carbon basis.

Intermediate identification using ¹³C labelled methanol: The methanol to olefin reaction using ¹³C labelled methanol as substrate was conducted simulating the real reaction condition. 150 mg pelletized sample (0.2-0.4 mm) was mixed with 2 g quartz (0.6-0.8 mm Fluka) before being introduced into the fix-bed reactor (7 mm diameter). N₂ (90 ml/min) was bubbled in methanol hold at -17°C, giving a WHSV=0.8 h⁻¹. The catalyst was first activated with a nitrogen flow of 80 ml/min for 1 h at 540°C, and then the temperature was decreased to reaction conditions (350°C). The feeding was stopped at 15 min time-on-stream and the reactor was cooled down to quench the reaction. Catalyst was loaded in glove box into rotor of ¹³C-NMR spectra for measurement.

Computational Details

All calculations in this work are based on density functional theory (DFT) and were carried out using the M062X functional⁴² and the 6-31g(d,p) basis set,^{43,44} as implemented in the Gaussian09 software.⁴⁵ In the study of the gas-phase reaction mechanism the positions of all C and H atoms in the cationic intermediates and transition states were fully optimized without restrictions, and all stationary points were characterized by means of frequency calculations. In a second step, two pure silica models of the RTH and CHA cavities, of composition Si₄₀O₆₀H₄₀ and Si₄₈O₇₈H₃₅, respectively, were constructed from the corresponding periodic structures. Interaction energies between the neutral cavity models and the cationic species involved in the gas-phase mechanisms were calculated as:

$$E_{int} = E(\text{cation}^+\text{-ZEO}) - E(\text{cation}^+) - E(\text{ZEO})$$

Where $E(\text{cation}^+\text{-ZEO})$ is the total energy of the cationic species inside the zeolite model, $E(\text{cation}^+)$ is the total energy of the isolated cation, and $E(\text{ZEO})$ is the total energy of the zeolite model. In these

calculations, the zeolite cavity model and the cationic hydrocarbon frameworks were kept rigid, and only the location of the cationic species within the cavity was optimized.

Data availability

All data is available from the authors upon reasonable request.

Acknowledgements

This work has been supported by the European Union through ERC-AdG-2014-671093 (SynCatMatch), the Spanish Government-MINECO through “Severo Ochoa” (SEV-2016-0683) and MAT2015-71261-R. The Electron Microscopy Service of the UPV is acknowledged for their help in sample characterization. C.L. acknowledges China Scholarship Council (CSC) for a Ph.D fellowship.

Author Contributions

A.C. conceived and directed the project. M.M. and A.C. designed the synthesis and M.M. directed the zeolite synthesis work. C.P. carried out the synthesis of the organic molecules. C.L. performed the zeolite synthesis. C.L. and J.M-T. performed the MTO catalytic experiments. M.B. carried out the theoretical calculations. M.M., M.B. and A.C. wrote the manuscript. C.L., C.P., J.M-T., M.B., M.M. and A.C. participated in the discussion and interpretation of the experimental data.

Competing interests

The authors declare no competing interests.

Fig. 1: MTO mechanisms. Proposed hydrocarbon pool mechanisms for the MTO reaction, including the paring and side-chain routes. Adapted from ref. ^{10,46}

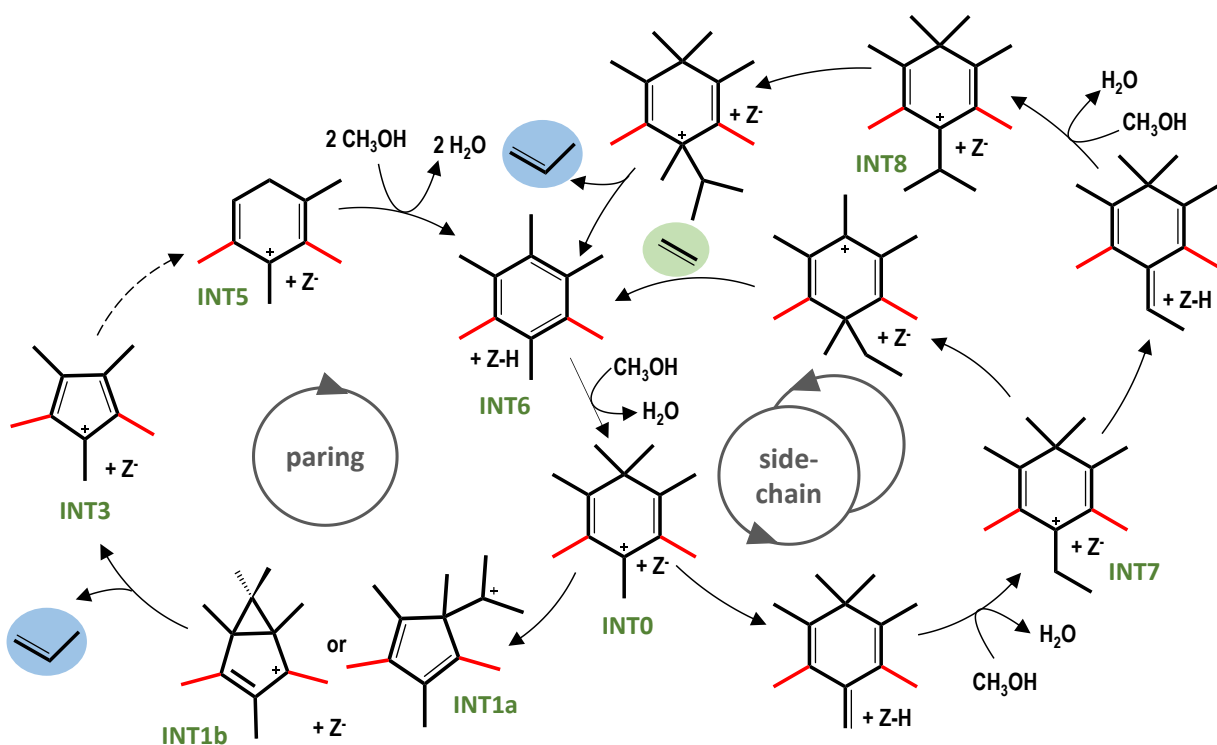


Fig. 2: OSDA mimics and zeolites. **a**, Proposed OSDA mimics of the different intermediates present in the HP paring route and, **b**, zeotypes obtained using these OSDA mimics

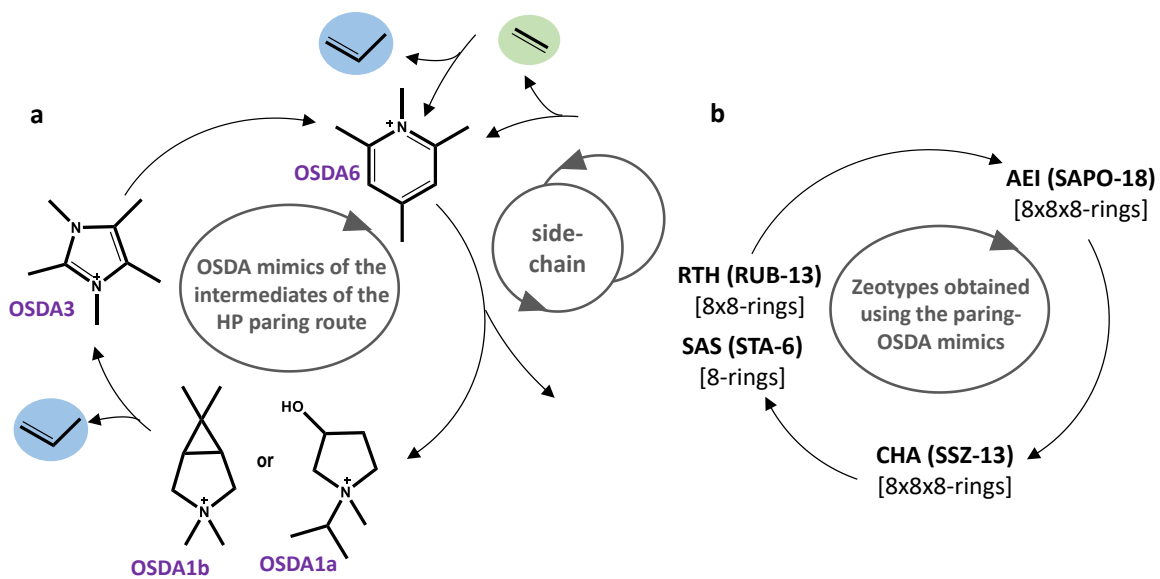


Fig. 3: Hydrocarbon species. a, b, ^{13}C CP/MAS NMR spectra of the retained organic species in the SSZ-13_std (a) and RUB-13 OSDA3 (b) zeolites after performing the MTO reaction using ^{13}C labelled methanol (**spinning sidebands*).

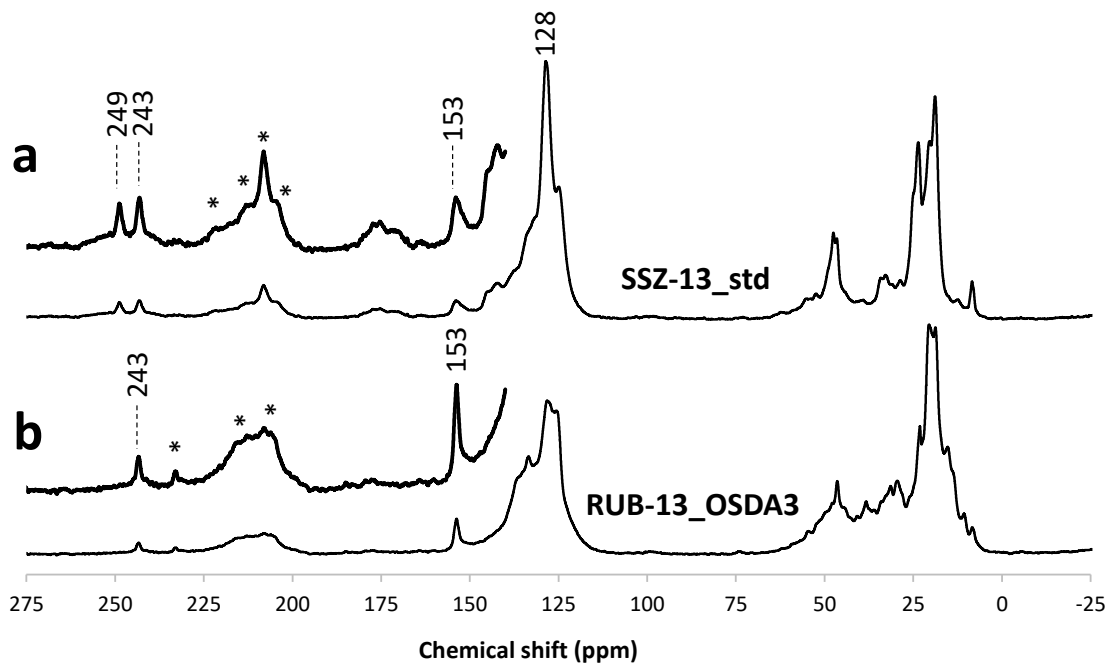


Fig. 4: Minimization of MTO intermediates within zeolite cavities. a,b, DFT optimized structures of INTO species in RTH (a) and CHA (b) cavity models. **c,d,** side view of INTO from HeptaMB⁺ (c) and PentaMB⁺ (d) within CHA cavity.

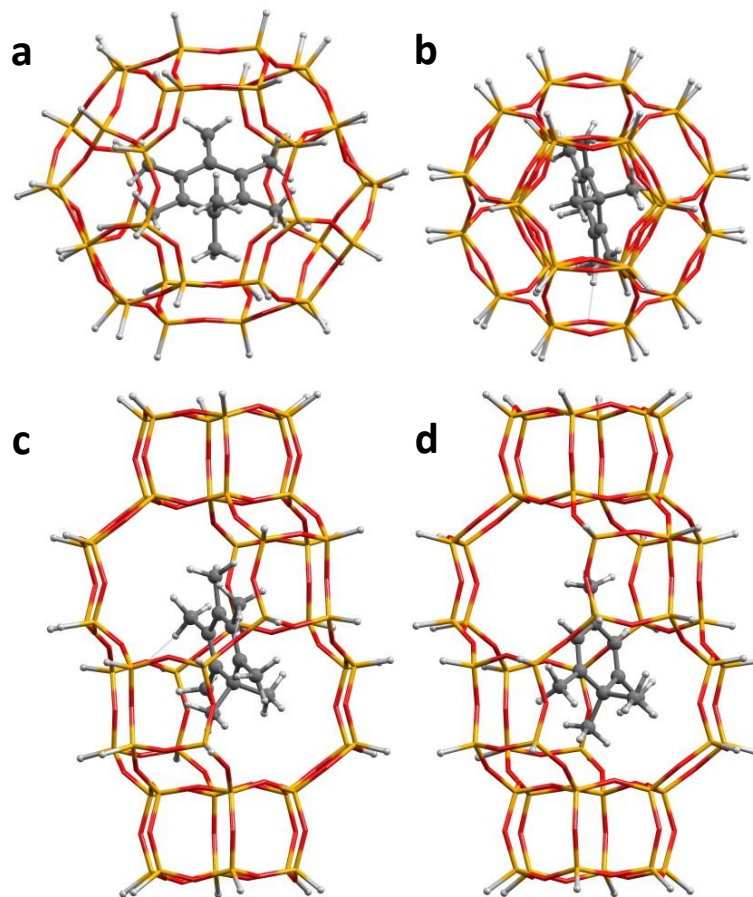


Fig. 5: Energy profiles for the paring routes. a,b, Calculated potential energy profiles for the first part of the paring route in RTH (blue) and CHA (red) models starting from PentaMB+ (a) and HeptaMB+ (b) cations.

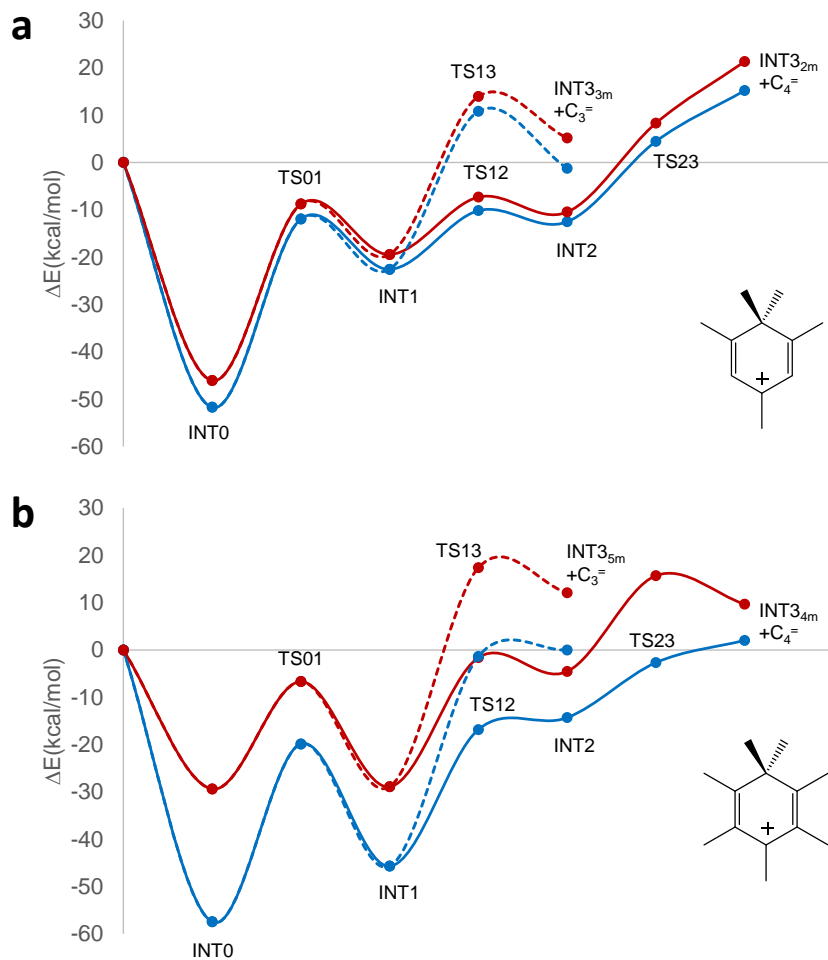
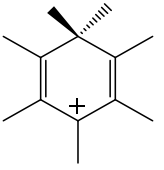
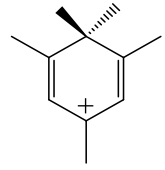


Table 1: Catalytic properties for the different small pore zeolites for MTO reaction (reaction conditions: T=350°C, WHSV=0.8 h⁻¹, w_{cat}=50 mg)

Sample	Structure	Catalyst lifetime (min)		Selectivity (%) at X ₉₅				
		X ₉₅	X ₅₀	C2 [≡]	C3 [≡]	C4 [≡]	C3 [≡] /C2 [≡]	C4 [≡] /C2 [≡]
SSZ-13_OSDA1a	CHA	50	75	40.8	37.8	5.6	0.92	0.14
SSZ-13_OSDA1b	CHA	1005	1360	45.2	34.4	10.9	0.76	0.24
RUB-13_OSDA3	RTH	270	645	14.7	45.1	24.7	3.07	1.68
SAPO-18_OSDA6	AEI	25	90	22.2	44.5	19.9	2.00	0.89
SSZ-13_std	CHA	212	311	39.3	37.8	15.4	0.96	0.39
SSZ-13_nano	CHA	472	757	43.2	37.4	14.2	0.86	0.33
SAPO-34_std	CHA	440	844	33.3	46.2	13.7	1.38	0.40

**Table 2: Stabilization of cationic intermediates and transition states by interaction with RTH and
CHA cavity models. DFT calculated interaction energies in kcal/mol.**

				
	RTH	CHA	RTH	CHA
INT0	-57,5	-29,4	-51,7	-46,1
TS01	-55,1	-42,1	-51,9	-48,7
INT1	-56,1	-39,3	-50,9	-47,8
TS12	-54,2	-39,0	-51,1	-48,2
INT2	-49,8	-40,1	-50,1	-48,1
T23	-54,5	-36,1	-52,3	-48,5
INT3 _{4m/2m} +C ₄ ⁼	-59,2	-51,6	-57,6	-51,5
TS13	-59,7	-40,9	-56,6	-53,3
INT3 _{5m/3m} +C ₃ ⁼	-57,5	-45,5	-63,3	-54,9
INT7	-51,7	-26,1	-42,4	-48,2
INT8	-25,8	-29,5	-21,2	-51,5

References:

- 1 Stocker, M. Methanol-to-hydrocarbons: catalytic materials and their behavior. *Micropor. Mesopor. Mater.* **29**, 3-48 (1999).
- 2 Tian, P., Wei, Y., Ye, M. & Liu, Z. Methanol to Olefins (MTO): From Fundamentals to Commercialization. *ACS Catal.* **5**, 1922-1938 (2015).
- 3 Ilias, S. & Bhan, A. Mechanism of the Catalytic Conversion of Methanol to Hydrocarbons. *ACS Catal.* **3**, 18-31 (2013).
- 4 Olsbye, U. *et al.* Conversion of Methanol to Hydrocarbons: How Zeolite Cavity and Pore Size Controls Product Selectivity. *Angew. Chem. Int. Ed.* **24**, 5810-5831 (2012).
- 5 Hemelsoet, K., Van der Mynsbrugge, J., De Wispelaere, K., Waroquier, M. & Van Speybroeck, V. Unraveling the Reaction Mechanisms Governing Methanol-to-Olefins Catalysis by Theory and Experiment. *ChemPhysChem* **14**, 1526-1545 (2013).
- 6 Song, W., Haw, J. F., Nicholas, J. B. & Heneghan, C. S. Methylbenzenes Are the Organic Reaction Centers for Methanol-to-Olefin Catalysis on HSAPO-34. *J. Am. Chem. Soc.* **122**, 10726-10727 (2000).
- 7 Arstad, B. & Kolboe, S. The Reactivity of Molecules Trapped within the SAPO-34 Cavities in the Methanol-to-Hydrocarbons Reaction. *J. Am. Chem. Soc.* **123**, 8137-8138 (2001).
- 8 Xu, T. *et al.* Synthesis of a Benzenium Ion in a Zeolite with Use of a Catalytic Flow Reactor. *J. Am. Chem. Soc.* **120**, 4025-4026 (1998).
- 9 Song, W., Nicholas, J. B., Sassi, A. & Haw, J. F. Synthesis of the Heptamethylbenzene cation in zeolite beta: in situ NMR and theory. *Catal. Lett.* **81**, 49-53 (2002).
- 10 Xu, S. *et al.* Direct observation of cyclic carbenium ions and their role in the catalytic cycle of the methanol-to-olefin reaction over chabazite zeolites. *Angew. Chem. Int. Ed.* **52**, 11564-11568 (2013).
- 11 Chen, J. *et al.* Elucidating the olefin formation mechanism in the methanol to olefin reaction over AIPO-18 and SAPO-18. *Catal. Sci. Tech.* **4**, 3268-3277 (2014).
- 12 Haw, J. F. *et al.* Roles for cyclopentenyl cations in the synthesis of hydrocarbons from methanol on zeolite catalyst HZSM-5. *J. Am. Chem. Soc.* **122**, 4763-4775 (2000).
- 13 Svelle, S. *et al.* Conversion of Methanol into Hydrocarbons over Zeolite H-ZSM-5: Ethene Formation Is Mechanistically Separated from the Formation of Higher Alkenes. *J. Am. Chem. Soc.* **128**, 14770-14771 (2006).
- 14 Teketel, S., Olsbye, U., Lillerud, K. P., Beato, P. & Svelle, S. Selectivity control through fundamental mechanistic insight in the conversion of methanol to hydrocarbons over zeolites. *Micropor. Mesopor. Mater.* **136**, 33-41 (2010).
- 15 Zhang, M. *et al.* Methanol conversion on ZSM-22, ZSM-35 and ZSM-5 zeolites: effects of 10-membered ring zeolite structures on methylcyclopentenyl cations and dual cycle mechanism. *RSC Adv.* **6**, 95855-95864 (2016).
- 16 Sassi, A. *et al.* Methylbenzene Chemistry on Zeolite HBeta: Multiple Insights into Methanol-to-Olefin Catalysis. *J. Phys. Chem. B* **106**, 2294-2303 (2002).
- 17 Sassi, A., Wildman, M. A. & Haw, J. F. Reactions of Butylbenzene Isomers on Zeolite HBeta: Methanol-to-Olefins Hydrocarbon Pool Chemistry and Secondary Reactions of Olefins. *J. Phys. Chem. B* **106**, 8768-8773 (2002).
- 18 Bjørgen, M., Olsbye, U., Petersen, D. & Kolboe, S. The methanol-to-hydrocarbons reaction: insight into the reaction mechanism from [12C]benzene and [13C]methanol coreactions over zeolite H-beta. *J. Catal.* **221**, 1-10 (2004).

- 19 McCann, D. M. *et al.* A Complete Catalytic Cycle for Supramolecular Methanol-to-Olefins Conversion by Linking Theory with Experiment. *Angew. Chem. Int. Ed.* **47**, 5179-5182 (2008).
- 20 Arstad, B., Kolboe, S. & Swang, O. Theoretical Study of the Heptamethylbenzenium Ion. Intramolecular Isomerizations and C2, C3, C4 Alkene Elimination. *J. Phys. Chem. A* **109**, 8914-8922 (2005).
- 21 De Wispelaere, K., Hemelsoet, K., Waroquier, M. & Van Speybroeck, V. Complete low-barrier side-chain route for olefin formation during methanol conversion in H-SAPO-34. *J. Catal.* **305**, 76-80 (2013).
- 22 Wang, C. M., Wang, Y. D. & Xie, Z. K. Verification of the dual cycle mechanism for methanol-to-olefin conversion in HSAPO-34: a methylbenzene-based cycle from DFT calculations. *Catal. Sci. Technol.* **4**, 2631-2638 (2014).
- 23 Wang, C. M., Wang, Y. D., Liu, H. X., Xie, Z. K. & Liu, Z. P. Theoretical insight into the minor role of paring mechanism in the methanol-to-olefins conversion within HSAPO-34 catalyst. *Micropor. Mesopor. Mater.* **158**, 264-271 (2012).
- 24 Ilias, S. & Bhan, A. The mechanism of aromatic dealkylation in methanol-to-hydrocarbons conversion on H-ZSM-5: What are the aromatic precursors to light olefins? *J. Catal.* **311**, 6-16 (2014).
- 25 Erichsen, M. W. *et al.* Conclusive Evidence for Two Unimolecular Pathways to Zeolite-Catalyzed De-alkylation of the Heptamethylbenzenium Cation. *ChemCatChem* **7**, 4143-4147 (2015).
- 26 Bhawe, Y. *et al.* Effect of Cage Size on the Selective Conversion of Methanol to Light Olefins. *ACS Catal.* **2**, 2490-2495 (2012).
- 27 Kang, J. H. *et al.* Further Studies on How the Nature of Zeolite Cavities That Are Bounded by Small Pores Influences the Conversion of Methanol to Light Olefins. *ChemPhysChem* **19**, 412-419 (2018).
- 28 Martin, N. *et al.* Nanocrystalline SSZ-39 zeolite as an efficient catalyst for the methanol-to-olefin (MTO) process. *Chem. Commun.* **52**, 6072-6075 (2016).
- 29 Dusselier, M., Deimund, M. A., Schmidt, J. E. & Davis, M. E. Methanol-to-Olefins Catalysis with Hydrothermally Treated Zeolite SSZ-39. *ACS Catal.* **5**, 6078-6085 (2015).
- 30 Yokoi, T., Yoshioka, M., Imai, H. & Tatsumi, T. Diversification of RTH-Type Zeolite and Its Catalytic Application. *Angew. Chem. Int. Ed.* **48**, 9884-9887 (2009).
- 31 Ji, Y., Deimund, M. A., Bhawe, Y. & Davis, M. E. Organic-Free Synthesis of CHA-Type Zeolite Catalysts for the Methanol-to-Olefins Reaction. *ACS Catal.* **5**, 4456-4465 (2015).
- 32 Liu, M. *et al.* Differences in Al distribution and acidic properties between RTH-type zeolites synthesized with OSDAs and without OSDAs. *Phys. Chem. Chem. Phys.* **16**, 4155-4164 (2014).
- 33 Gallego, E. M. *et al.* "Ab initio" synthesis of zeolites for preestablished catalytic reactions. *Science* **355**, 1051-1054 (2017).
- 34 Zones, S. I. & Nakagawa, Y. Use of Modified Zeolites as Reagents Influencing Nucleation in Zeolite Synthesis. *Stud. Surf. Sci. Catal.* **97**, 45-52 (1995).
- 35 Li, C., Moliner, M. & Corma, A. Building zeolites from pre-crystallized units: nanoscale architecture. *Angew. Chem. Int. Ed.* DOI: **10.1002/anie.201711422** (2018).
- 36 Zones, S. I. Zeolite SSZ-13 and its method of preparation. *U.S. Patent Nr. 4,544,538* (1985).
- 37 Li, Z., Navarro, M. T., Martínez-Triguero, J., Yu, J. & Corma, A. Synthesis of nano-SSZ-13 and its application in the reaction of methanol to olefins. *Catal. Sci. Technol.* **6**, 5856-5863 (2016).

- 38 Kumar, M., Luo, H., Román-Leshkov, Y. & Rimer, J. D. SSZ-13 Crystallization by Particle Attachment and Deterministic Pathways to Crystal Size Control. *J. Am. Chem. Soc.* **137**, 13007-13017 (2015).
- 39 Martínez-Franco, R., Cantin, A., Moliner, M. & Corma, A. Synthesis of the Small Pore Silicoaluminophosphate STA-6 by Using Supramolecular Self-Assembled Organic Structure Directing Agents. *Chem. Mater.* **26**, 4346-4353 (2014).
- 40 Schmidt, J. E., Deimund, M. A., Xie, D. & Davis, M. E. Synthesis of RTH-Type Zeolites Using a Diverse Library of Imidazolium Cations. *Chem. Mater.* **27**, 3756-3762 (2015).
- 41 Moliner, M., Franch, C., Palomares, E., Grill, M. & Corma, A. Cu-SSZ-39, an active and hydrothermally stable catalyst for the selective catalytic reduction of NOx. *Chem. Commun.* **48**, 8264-8266 (2012).
- 42 Zhao, Y. & Truhlar, D. G. The M06 suite of density functionals for main group thermochemistry, thermochemical kinetics, noncovalent interactions, excited states, and transition elements: two new functionals and systematic testing of four M06-class functionals and 12 other functionals. *Theor. Chem. Acc.* **120**, 215-241 (2008).
- 43 Ditchfield, R., Hehre, W. J. & Pople, J. A. Self-Consistent Molecular Orbital Methods. 9. Extended Gaussian-type basis for molecular-orbital studies of organic molecules. *J. Chem. Phys.* **54**, 724-728 (1971).
- 44 Hehre, W. J., Ditchfield, R. & Pople, J. A. Self-Consistent Molecular Orbital Methods. 12. Further extensions of Gaussian-type basis sets for use in molecular-orbital studies of organic-molecules. *J. Chem. Phys.* **56**, 2257-2261 (1972).
- 45 Frisch, M. J. *et al.* Gaussian 09, Revision C.01. *Gaussian, Inc., Wallingford CT*, (2009).
- 46 Van Speybroeck, V. *et al.* First principle chemical kinetics in zeolites: the methanol-to-olefin process as a case study. *Chem. Soc. Rev.* **43**, 7326-7357 (2014).